Materials Characterization 162 (2020) 110228

Contents lists available at ScienceDirect

Materials Characterization

journal homepage: www.elsevier.com/locate/matchar

Effects of yttrium oxides on the microstructure and mechanical properties of 15-15Ti ODS alloy fabricated by casting

Yan Zhuang[a], Xinyue Zhang[b], Tao Peng[a], Huiyang Fan[a], Xiaoxin Zhang[a,c], Qingzhi Yan[a,*], Alex A. Volinsky[d]

[a] Institute of Nuclear Materials, School of Materials Science and Engineering, University of Science and Technology Beijing, Beijing 100083, China
[b] National Engineering Laboratory for Modern Materials Surface Engineering Technology, Guangdong Institute of New Materials, Guangzhou 510651, China
[c] Key Laboratory of Optoelectronic Devices and Systems of Ministry of Education and Guangdong Province, College of Optoelectronic Engineering, Shenzhen University, Shenzhen 518060, China
[d] Department of Mechanical Engineering, University of South Florida, Tampa, FL 33620, USA

ARTICLE INFO

Keywords:
ODS
15-15Ti
Casting
Yttrium oxides
Dispersion
Mechanical properties

ABSTRACT

The emphasis of oxide dispersion strengthened (ODS) steels is on the size, morphology, and distribution of the oxide particles. In this paper, the behavior of yttrium oxides particles in 15-15Ti alloy fabricated by casting was systematically investigated, and the microstructure of as-rolled, solid solution and as-recrystallized specimens was characterized. The X-ray diffraction results indicated that the secondary phases in 15-15Ti alloy are composed of $YTaO_4$, $YFeO_3$, Y_2O_3 and metal carbides. The thermodynamic simulation results and the observed microstructure suggest that the coarsening and agglomeration of yttrium oxides occurred during solidification. After 80% cold rolling and recrystallization annealing, yttrium oxides were refined and distributed more uniformly with typical sizes of about 50–100 nm. As a result, the microstructure of 15-15Ti alloy with dispersed yttrium oxides particles was achieved. Compared with the conventional 15-15Ti alloy (3.67 alloy), new 15-15Ti alloy has a higher ultimate tensile strength of 690 MPa and yield strength of 523 MPa. Accordingly, these results indicated that 15-15Ti alloy exhibited excellent mechanical properties.

1. Introduction

Oxide dispersion strengthened (ODS) steels are candidate materials for generation IV reactors. Due to their high creep strength and excellent irradiation resistance, ODS steels have been attracting increased attention [1,2]. Stable and fine yttrium oxide particles were introduced well dispersed in ODS steels, acting as pinning points to hinder the grain boundary sliding, dislocation motion, and vacancies caused by irradiation damage [3]. Most of the existing investigations of yttrium oxide particles mainly focused on ferritic and ferritic/martensitic stainless steels prepared by mechanical alloying (MA). Among these studies, Kim et al. [4] found that the high density of fine yttrium oxide particles in the ferritic/martensitic ODS steel promoted excellent mechanical properties. Saimon-Legagneur et al. [5] have also observed many fine yttrium oxide particles in the ferritic and ferritic/martensitic ODS steels and reported that these steels had high recrystallization resistance. Odette et al. [6] discovered that the ultrahigh density fine yttrium oxide particles in the ferritic/martensitic ODS steel could trap He in fine-scale bubbles and suppress void swelling during irradiation. However, most of the ODS steels literature reports focused on fine yttrium oxide particles with a ferritic/martensitic matrix prepared by MA [7–9], which still suffered from poor oxidation and corrosion resistance [10,11]. Nevertheless, there have been few literature reports about austenitic ODS steels. 15-15Ti steel as an austenitic steel has an outstanding combination of overall high-temperature properties, oxidation, and corrosion resistance [12]. The 15-15Ti alloy with yttrium oxides particles is considered promising to overcome the above-mentioned problems in the ferritic and ferritic/martensitic ODS steels. In this case, we focus on the problems with 15-15Ti alloy with yttrium oxides particles, as listed below.

1. Generally, the ODS steels are manufactured via MA. However, MA is difficult for the batch production and prohibitively expensive for the large-scale production [13,14]. Casting is an alternative explored method. However, it is also difficult due to the agglomeration of yttrium oxides and coarsening. Baghchesara et al. [15] fabricated Al-MgO nanocomposite by casting and powder metallurgy methods. Compared with the powder metallurgy, Casting is a cheap, simple,

* Corresponding author.
E-mail address: qzyan@ustb.edu.cn (Q. Yan).

https://doi.org/10.1016/j.matchar.2020.110228
Received 18 August 2019; Received in revised form 29 January 2020; Accepted 24 February 2020
Available online 25 February 2020

and efficient method. Beygi et al. [16] prepared Al-Al_2O_3 nanocomposite by casting successfully and increased the weight percentage of nano Al_2O_3 particles. Park et al. [17] fabricated carbon steel dispersed with nano-sized TiC ceramic particles by casting, hot rolling, cold rolling and heat treatment. Verhiest et al. [18] manufactured ferritic/martensitic ODS steel by casting and rapid solidification. Recently, Hong et al. [19] reported a new casting method to prepare 9Cr-ODS steel with 0.2–2 μm yttrium oxide particles using Y and Fe_2O_3 as oxygen carrier.

2. As described above, the size, morphology, and distribution of yttrium oxide particles severely affect the properties of ODS steels. Most studies have focused on the interactions of yttrium oxides with the matrix under high-resolution microscopy observations [1–12]. Nevertheless, there are almost no data available on the distribution of yttrium oxides, especially under low magnification.

Therefore, in this paper, we manufactured 15-15Ti alloy with dispersed yttrium oxide particles of 50–100 nm size using the casting method and conventional processing. To date, the distribution of yttrium oxides in 15-15Ti alloy has not been characterized. The objective of this research was to explore the behavior of yttrium oxides in 15-15Ti based steel via casting illustrated by SEM and TEM under low and high magnification. The systematic studies were carried out to investigate microstructure and subsequent properties of 15-15Ti with yttrium oxides particles Microstructure characterization of yttrium oxides together with effects of yttrium oxides on mechanical properties can be useful for further development of 15-15Ti alloy.

2. Experimental

Before casting, Fe_2O_3 powders were placed at the bottom of the mold and isothermal treatment was applied for 10 min [20]. The 15-15Ti alloy was prepared by vacuum induction melting with nominal composition listed in Table 1. Metallic Y powders were added to the melt. The melt was poured into the mold when metallic Y powder dissolved into the melt. Y would in situ react with activated O from Fe_2O_3 during the casting due to yttrium is strong oxygen forming element. The yttrium oxides was generated. Then the 50 kg ingot was forged into a bar with the cross-section of 90 mm × 60 mm and subsequently hot rolled into a 15 mm thick plate. The as-rolled (ROL) specimens were cut from the plate. The ROL samples were solid solution treated at 1200 °C for 1 h and cooled in water to form the solid solution (SOL) specimens. After solid solution treatment, plates with a thickness of 15 mm were cut into slabs, which were then subjected to 80% cold rolling. The as-recrystallized (REC) specimens were treated at 850 °C for 4 h and cooled in water after 80% cold rolling.

To identify the secondary phases in 15-15Ti alloy, the secondary phases were extracted from the specimens by the electrolytic method. The secondary phases analysis was performed by X-ray diffraction (XRD) at 1°/min 2θ scan rate. In order to predict the secondary phases crystallization sequence during solidification, thermodynamic calculations were carried out using the Thermo-Calc software. The microstructure of the specimens was observed by scanning electron microscopy (SEM) with energy dispersive spectroscopy (EDS) detector and transmission electron microscopy (TEM). The acceleration voltage, electron beam diameter, and beam current used in these experiments were 20 kV, 10 nm, and 80 μA, respectively. All SEM images were secondary electron images. The specimens were mechanically polished and etched with 10% nitric acid +90% hydrofluoric acid aqueous solution. Carbon foil TEM specimens were mechanically polished and electrochemically thinned using 10% perchloric acid +90% methanol. Tensile tests were carried out using the MTS809 machine at a strain rate of 3.2×10^{-4} s^{-1} at room temperature, using tensile samples with a gauge length of 15 mm.

The grain size was statistically measured by quantitative metallography method. The number density of the secondary phase was obtained by Image J software with the equation as followed [13]:

$$N_A = \frac{N}{A} \quad (1)$$

where N_A is the areal number density, N is the number of particles in SEM image and A is the area of the image.

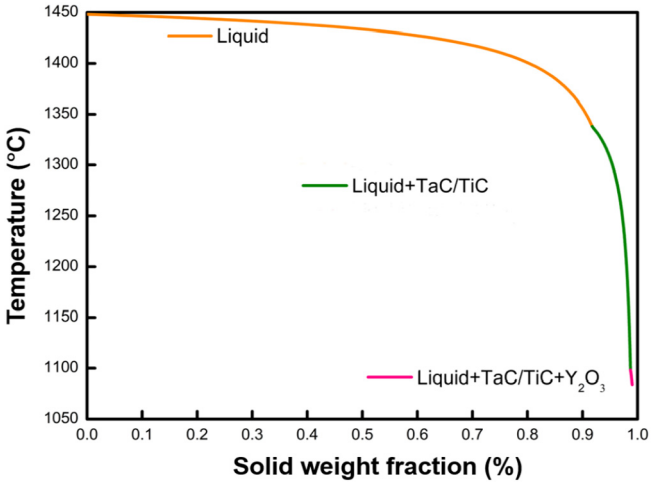

Fig. 1. The sequence of secondary phases formation in 15-15Ti alloy during solidification based on thermodynamic calculations.

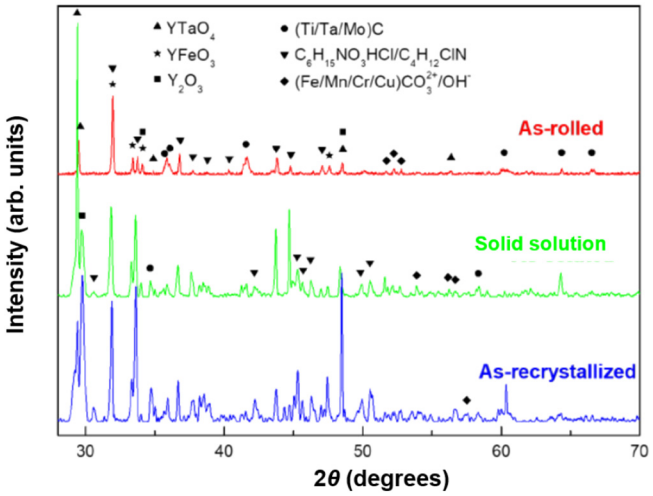

Fig. 2. X-ray diffraction patterns of the secondary phases in the 15-15Ti alloy.

Table 1
The nominal chemical composition of 15-15Ti alloy (wt%).

C	Cr	Ni	Mo	Ti	Mn	Si	Y	Ta	Al	V	N	S	P	Fe
0.04	15	15	2.2	0.2	1.5	0.5	0.6	0.1	< 0.05	< 0.01	< 0.01	< 0.05	< 0.05	Bal

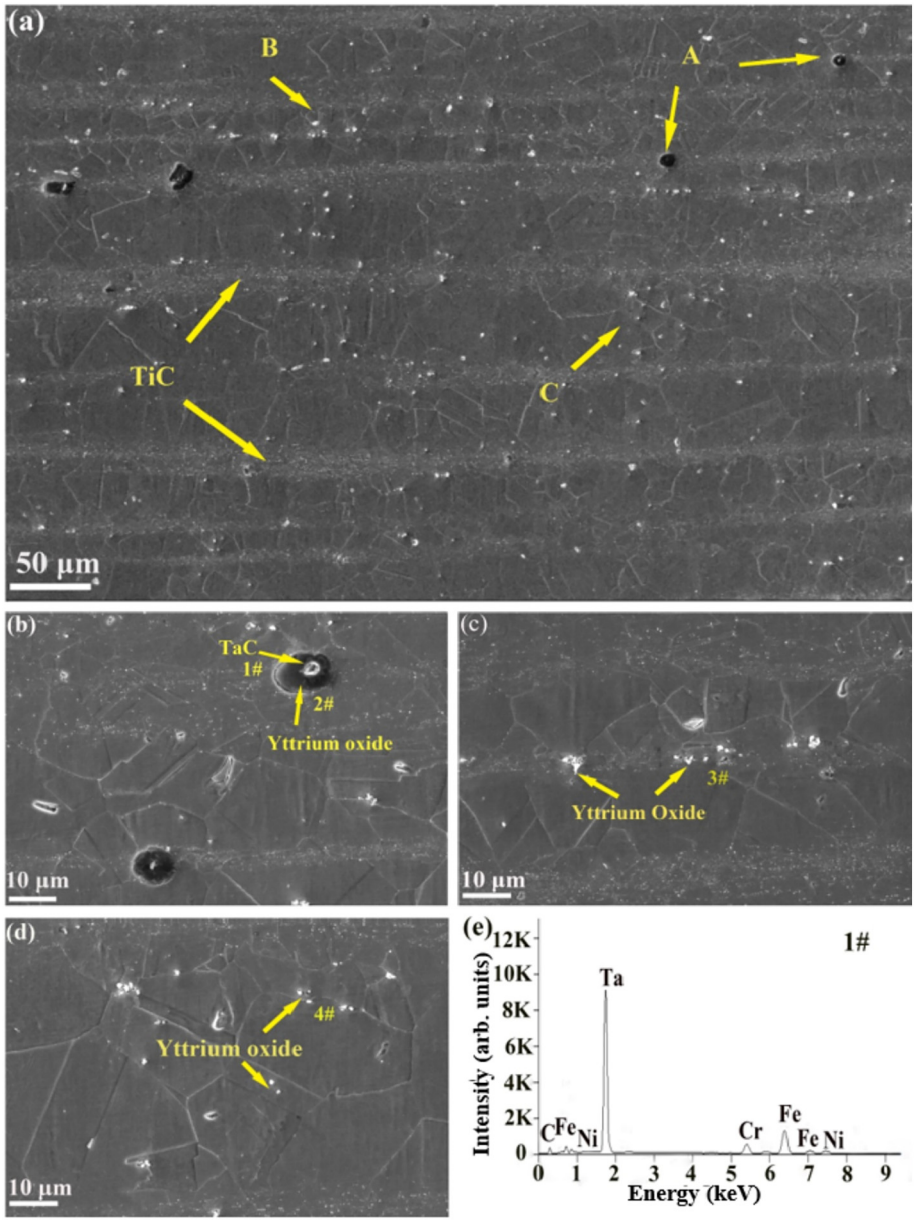

Fig. 3. The microstructures of the ROL specimen with polishing and etching: (a) SEM image of the ROL specimen; (b) The typical morphology of yttrium oxide/TaC; (c) Agglomerated yttrium oxide particles aligned along the rolling direction; (d) Fine yttrium oxide particles and agglomerated yttrium oxide particles; (e) EDS microanalysis of the spot 1#; (f) EDS microanalysis of the spot 2#; (g) EDS microanalysis of the spot 3#; (h) EDS microanalysis of the spot 4#.

3. Results and discussion

3.1. Microstructure

In order to estimate the formation sequence of yttrium oxides in 15-15Ti alloy during solidification, the thermodynamic calculations were carried out and the results are shown in Fig. 1. The solidification process of the 15-15Ti alloy could be simulated using the Scheil-Gulliver model realized in the Thermo-Calc software. The design composition was used as the initial composition during solidification. According to the simulation results based on the concentration equilibrium, the final constituents of 15-15Ti alloy were the austenite matrix, TaC, TiC and Y_2O_3 after solidification. TaC would be solidified ahead of Y_2O_3. TaC precipitated earlier when the nucleation condition has achieved. The secondary phases nucleate successively during solidification.

XRD patterns of the secondary phases in 15-15Ti alloy are presented in Fig. 2. The XRD reflections of $C_6H_{15}NO_3HCl/C_4H_{12}ClN$ and (Fe/Mn/Cr/Cu)CO_3^{2+}/OH^- in Fig. 2 are from the electrolyte and electrode. In the SOL specimen, the $YTaO_4$ XRD intensity is the strongest. The minor secondary phases are metal carbides (MC). The three XRD patterns are similar. Compared with the ROL specimen, following solid solution treatment, the X-ray diffraction reflection intensity of $YTaO_4$ increases significantly, while the reflection intensity of MC reduces, which can be attributed to the increase in the $YTaO_4$ content and decrease in the MC content for SOL specimen. Following solid solution treatment, the diffusivity of C increased. With the higher diffusivity, most MC particles dissolve into the matrix. Therefore, the content of $YTaO_4$ increases considerably in SOL specimen. The variation trend of XRD patterns is consistent with the microstructure. The related analysis will be discussed below based on the microstructure. The XRD patterns reveal that for the ROL, SOL and REC specimens, the major secondary phases are the oxides of yttrium, including $YTaO_4$, $YFeO_3$, and Y_2O_3.

$YTaO_4$, $YFeO_3$, and Y_2O_3 are typically stable yttrium oxides. As reported by Hong et al. [20], Peng et al. [21], and Mathur et al. [22],

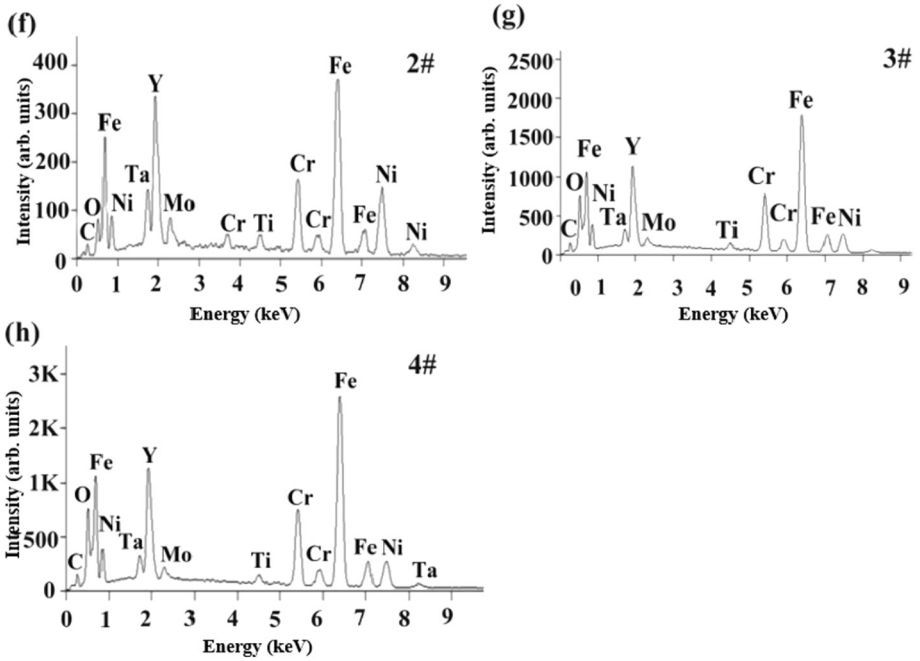

Fig. 3. (*continued*)

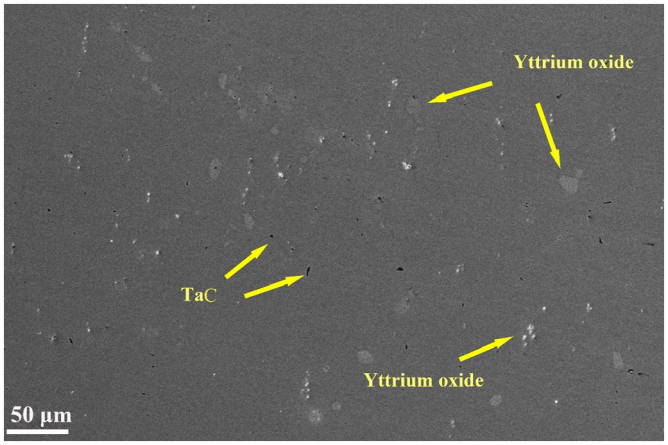

Fig. 4. The microstructure of the SOL specimen with polishing.

these yttrium oxides can be generated in the following ways:

$$4Y + 3O_2 \rightarrow 2Y_2O_3 \quad (2)$$

$$Y_2O_3 + Ta_2O_5 \rightarrow 2YTaO_4 \quad (3)$$

$$Y_2O_3 + Fe_2O_3 \rightarrow 2YFeO_3 \quad (4)$$

The micrographs with EDS for all conditions indicate the presence of many yttrium oxide particles. Fig. 3(a) shows the microstructure of the ROL specimen at low magnification. There are four typical kinds of morphology in these specimens. First, some black spots with the typical size of about 10 μm can be observed, with small embedded particles clearly seen in Fig. 3(b) at a higher magnification. The black spots and the small particles are the yttrium oxides and TaC, respectively (Fig. 3(e) and (f)). Second, as seen in Fig. 3(c) and (d), the agglomerated yttrium oxides (Fig. 3(g)) are aligned along the rolling direction or have random distribution with a typical particle size of 3–5 μm. Third, in Fig. 3(d), there are smaller secondary phases (< 500 nm) with a spherical shape in grains and at grain boundaries. Most of the particles were identified as yttrium oxides by EDS in Fig. 3(h). The number density of yttrium oxides in the ROL specimen is about 1011 mm^{-2}. In Fig. 3(a), the reversal in contrast between the black yttrium oxide spots and white agglomerated yttrium oxides was attributed to different phase compositions. It will be discussed as below. There are also extremely fine 20 nm TiC particles present in the ROL specimen. It can be also seen from Fig. 3(a) that the distribution of TiC is aligned along the rolling direction.

The coarsening and agglomeration of yttrium oxides can be explained by the excessive content of yttrium and oxygen. As described above, the ROL specimen forms three types of yttrium oxides during solidification and hot rolling process. The oxygen content aligned with yttrium. During melting, burning loss of yttrium leads to higher oxygen content. As indicated in the Fe—O phase diagram [16], the larger content of oxygen would lead to a higher liquidus temperature, resulting in larger distance from the liquidus to the eutectic lines. Therefore, yttrium oxide particles would have formed earlier, then further developed and grew larger during the solidification. This is also consistent with the literature reports [20,23,24]. In addition, particles tend to float due to lower density compared with Fe [25]. With the addition of excessive yttrium, some yttrium oxide particles nucleated earlier and decreased the concentration of yttrium in liquid steel. Besides, yttrium oxide particles will tend to float due to their lower density than Fe. The floating yttrium oxide particles serve as the nucleation sites. Driving force and minimization of the interfacial energy contribute to diffusion and nucleation of yttrium in the liquid steel around floating yttrium oxide particles [26]. Consequently, this resulted in coarsening and agglomeration of yttrium oxide particles.

We next examined the distribution and morphology of the secondary phases in the SOL specimen. As shown in Fig. 4, after solid solution treatment, most of the extremely fine TiC particles that are aligned along the rolling direction dissolved into the matrix as demonstrated by the XRD patterns. In SOL specimen, the remaining yttrium oxides exist in the two forms: the agglomeration of yttrium oxides and the black spots with TaC particles inside. The $YTaO_4$ and the agglomerated Y_2O_3 particles were too coarse to dissolve in the matrix. The number density of yttrium oxides in the SOL specimen is about 487 mm^{-2}. We also found that the diffraction intensity of $YTaO_4$ increased with dissolving of TiC in Fig. 2. Accordingly, it can be speculated that the black spots in ROL specimen of the remaining yttrium oxide are $YTaO_4$. As described above, TaC would be solidified ahead of Y_2O_3. Together with the EDS results in Fig. 3(e), this can account for the

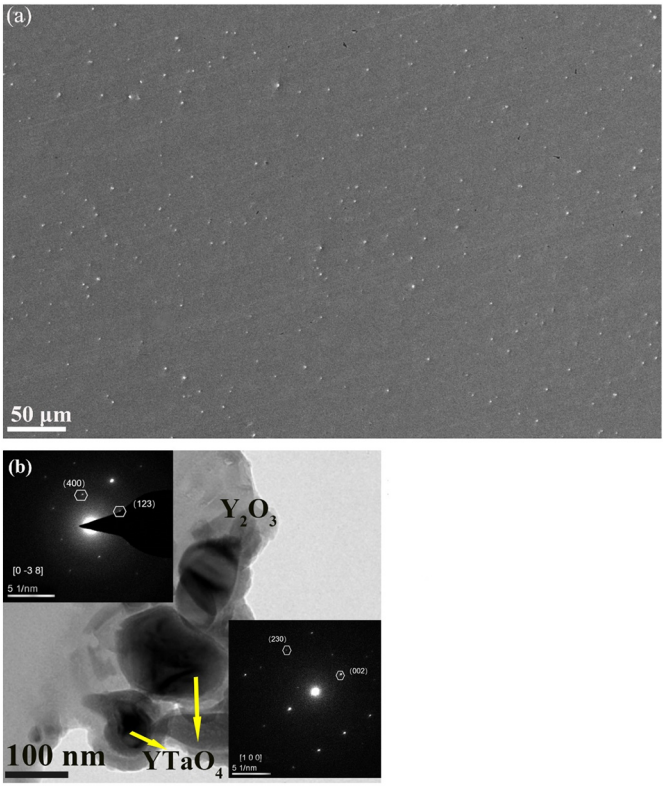

Fig. 5. The microstructure of the REC specimen with polishing: (a) SEM image of the REC specimen; (b) TEM images and the selected area diffraction of yttrium oxide particles.

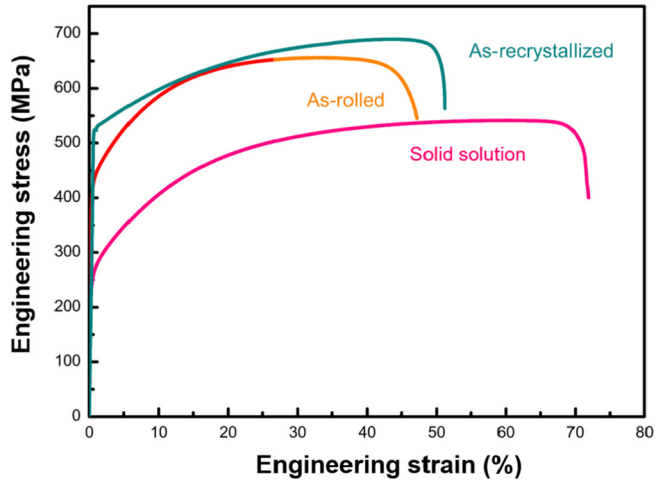

Fig. 6. Tensile engineering strain-stress curves of the 15-15Ti alloys at room temperature.

Table 2
The tensile properties of 15-15Ti alloy.

Specimen	Grain size μm	Ultimate tension strength MPa	Yield strength MPa	Total elongation %
REC	2–4	690	523	50.8
SOL	52	541	237	71.5
ROL	22–46	656	406	47.1
15-15Ti (3.67alloy) [31]	20–43	635	325	48.0

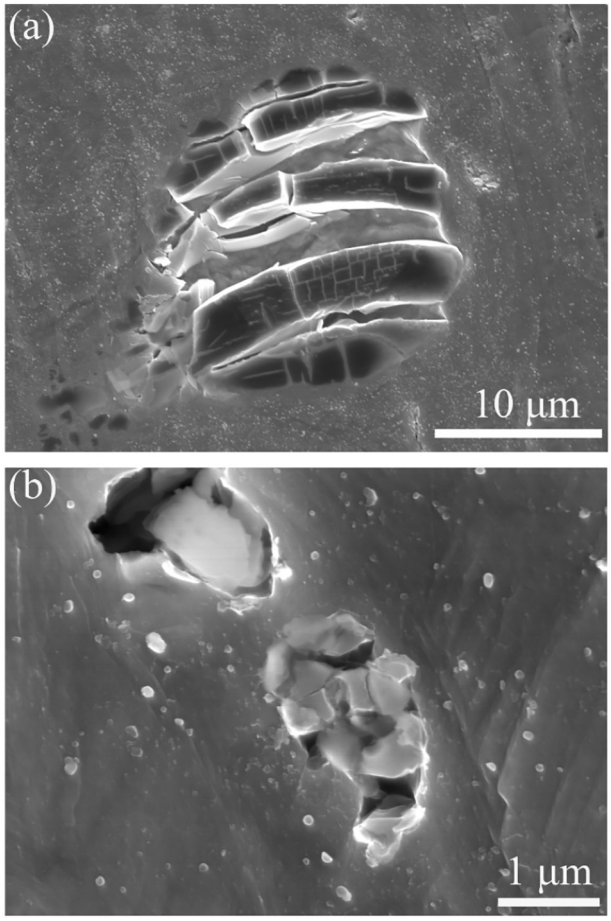

Fig. 7. SOL specimen: (a) coarsened yttrium oxide particles and (b) agglomerated yttrium oxide particles after tensile testing.

heterogeneous nucleation of the black spots. TaC serves as the heterogeneous nucleation sites and $YTaO_4$ nucleates around TaC.

The distribution and morphology of the secondary phases in REC specimen can be clearly seen in Fig. 5. After 80% cold deformation and complete recrystallization annealing, it can be observed that the average size of yttrium oxide particles is smaller in Fig. 5a. The secondary phases of yttrium oxides were identified as $YTaO_4$ and Y_2O_3 by selected area diffraction pattern in Fig. 5(b). The size of $YTaO_4$ and Y_2O_3 is about 100 nm. The number density of yttrium oxides in the REC specimen is about 1508 mm^{-2}, which is more than three times the number density in the SOL specimen. This indicates that coarsening and agglomeration of yttrium oxide particles were broken into fine particles with the typical sizes of about 50–100 nm in the REC specimen, distributed more uniformly.

The examination of the REC specimen revealed that yttrium oxides were fine and distributed more uniformly. Previous studies have analyzed the deformation and recrystallization processes of refined secondary phases. First, the activation of basal and non-basal slip system promotes the plastic deformation [27]. However, the secondary phases block the movements of dislocations. This causes high stress concentration at the interface between the matrix and the secondary phases. The large difference in the elastic modulus leads to the deformation inconsistency [28]. Then cracks start with local high stress concentration around the coarsening secondary phases, such as $YTaO_4$ and aggregated Y_2O_3. The coarsened secondary phases and interfaces gradually were broken up due to cracks propagating through them [29]. With further deformation, in order to minimize the surface energy, the broken particles spheroidized and distributed more homogeneously [30]. Finally, the broken interfaces would be healed by the

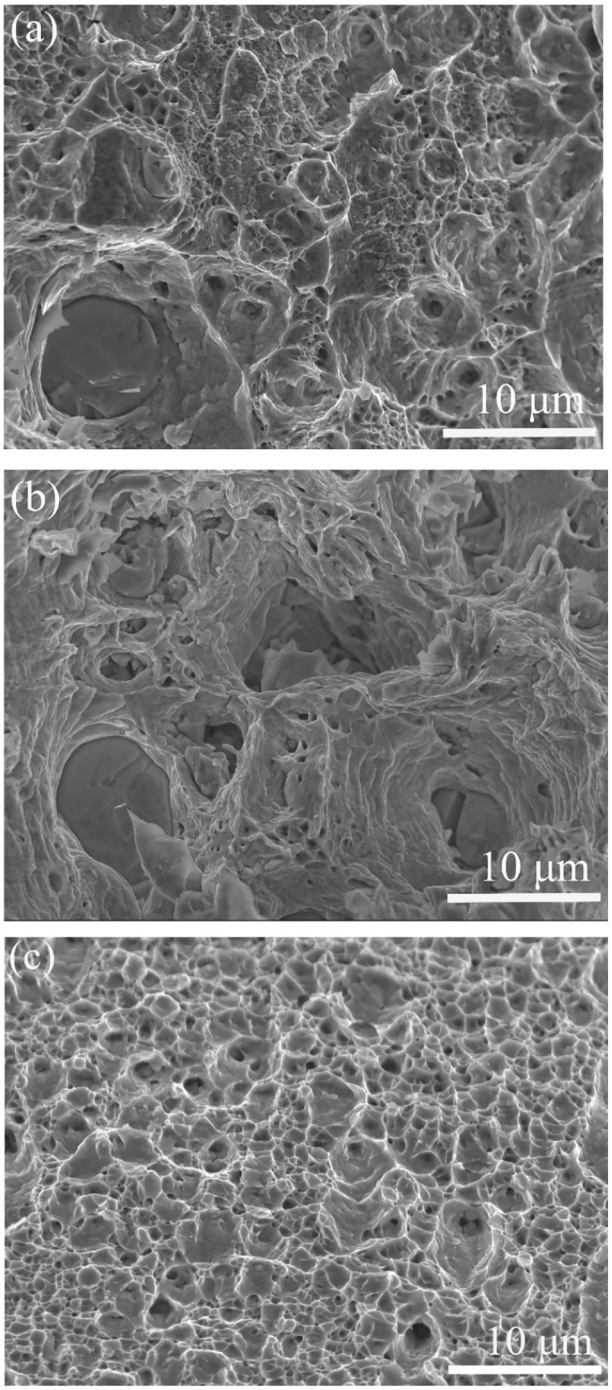

Fig. 8. Tensile fracture of 15-15Ti alloy: (a) The ROL specimen; (b) The SOL specimen; (c) The REC specimen.

thermal treatment process [31]. Due to the large difference in elastic modulus between the austenitic matrix and yttrium oxide particles as the ceramic phase, the large yttrium oxide particles in REC specimen became smaller as a result of large deformation and recrystallization. Fig. S2 shows the finer dispersion of secondary phase particles in REC specimen. There are a large number of particles in Fig. S2(a), and the image of partial enlargement of finer yttrium oxide particles (< 10 nm) is shown in Fig. S2(b) with the corresponding EDS pattern in Fig. S2(c).

3.2. Mechanical properties

In order to understand the effects of yttrium oxide particles on the mechanical properties of 15-15Ti alloy, the engineering stress-strain curves at room temperature were obtained for the ROL, SOL and REC specimens, as shown in Fig. 6. The results of the tensile tests are summarized in Table 2. The 15-15Ti alloy in all conditions shows fine plasticity with the elongation of the steel of > 45%, which is close to the 15-15Ti alloy (3.67 alloy) with similar grain size and composition, as reported in the literature [32]. From these results, it can be concluded that yttrium oxides as secondary phases of the ROL specimen would increase the ultimate tensile strength and the yield strength. Compared with 315 MPa yield strength of the 15-15Ti alloy (3.67 alloy) with similar grain size and composition [32], the ultimate tensile strength increased from 635 MPa to 656 MPa, and the yield strength increased from 325 MPa to 406 MPa with the addition of yttrium oxides. The most impressive data are from the REC specimens. Compared with the 325 MPa yield strength of the 15-15Ti alloy (3.67 alloy), the yield strength of the REC specimen reached 523 MPa. The yield strength increased by almost 100 MPa.

The results in Table 2 indicate that yttrium oxides greatly strengthened new 15-15Ti steel but did not cause serious embrittlement. To analyze the change of the mechanical properties with standard experimental processes, the mechanical properties of new 15-15Ti alloy were further compared with the 15-15Ti alloy (3.67 alloy). The obtained ROL, SOL and REC specimens were processed by hot rolling, solid solution treatment, cold deformation, and complete recrystallization annealing, respectively. With the similar grain size, the yield strength of the ROL specimen increased by almost 100 MPa due to dispersion strengthening caused by the fine yttrium oxides. However, the improvement was still limited. In order to eliminate this effect, TiC particles decomposed and dissolved into the matrix by the solid solution treatment in SOL specimen. The remaining was the agglomeration of yttrium oxides and coarsening of $YTaO_4$ particles. From Fig. 7(a) and (b), it is evident that brittle cracking was initiated around coarsened $YTaO_4$ particles and the aggregation of yttrium oxides as described above in SOL specimen. The solid solution strengthening was weakened.

After cold deformation and complete recrystallization annealing, the yield strength of the REC specimen was clearly increased, compared with the 15-15Ti alloy (3.67 alloy). The improvement in the strength could be caused by at least three factors: grain refinement strengthening, reducing secondary phases coarsening and fine secondary phases strengthening. First, when the grain size of the REC specimen decreased to 2–5 μm, the yield strength would readily improve by means of the well-known Hall-Petch effect [33]. Furthermore, the agglomeration of yttrium oxides and coarsened $YTaO_4$ particles in ROL and SOL specimen were broken into fine particles. This reduced the cleaved coarsened particles effects on the matrix [34]. Besides that, the large size coarsened particles were broken into a high density of fine particles distributed more uniformly. The dispersive particles act as pinning points for migration of grain boundaries and dislocation motion leading to the high yield strength.

To observe yttrium oxide particles during fracture, the images of tensile fracture surfaces were collected for the ROL, SOL and REC specimens (Fig. 8(a)-(c)). The fracture surface of the ROL specimen is composed of lamellar cleavage planes and some of the small dimples as seen in Fig. 8(a). The SOL specimen in Fig. 8(b) shows mainly lamellar cleavage planes with very few small dimples in the fracture surface of the ROL specimen. However, the fracture surface of the REC specimen is almost entirely composed of small and deep dimples (Fig. 8(c)). Fig. 7(a) presents the coarsened 10 μm particles with cracks inside. Fig. 7(b) shows the agglomeration of small particles which are separated from cracks. They were identified as yttrium oxides. These two types of particles, which can be found both in the ROL and SOL specimens (Figs. 3 and 4), broke during tensile testing and acted as sources of cracks. Therefore, the REC specimen presents good ductility compared with the fractography of the other two specimens.

4. Conclusions

In summary, new 15-15Ti alloy with 50–100 nm and dispersed yttrium oxides was successfully manufactured via casting and subsequent conventional processing. It can be concluded that:

(1) Yttrium oxides particles in 15-15Ti alloy by casting were identified as $YTaO_4$, $YFeO_3$, and Y_2O_3.
(2) Heterogeneous nucleation occurred between TaC and yttrium oxides. The typical size of $YTaO_4$ was about 10 μm, the agglomeration of yttrium oxides was about 3–5 μm and smaller yttrium oxides (< 500 nm) with spherical shapes were found in grains and at grain boundaries. The thermodynamic simulation results suggested that the coarsening and agglomeration of yttrium oxides happened during solidification.
(3) After 80% cold rolling and recrystallization annealing, yttrium oxides were refined into particles with the typical sizes of about 50–100 nm distributed more uniformly.
(4) Under the effects of grains refinement and dispersion strengthening, the mechanical properties of yttrium oxides were significantly improved compared with the 15-15Ti alloy (3.67 alloy). The ultimate tensile strength of new 15-15Ti alloy increased to 690 MPa, while the yield strength increased to 523 MPa.
(5) The excessive addition of yttrium in 15-15Ti steel (0.6 wt%) resulted in the coarsening and agglomeration of yttrium oxides.

This work primarily studied the 15-15Ti alloy with yttrium oxides particles fabricated by casting, which may be a promising candidate material in generation IV reactors. As a simple, cheap and efficient method, the study on casting method would contribute to the development and optimization of materials used in fast reactors. We will focus on refining the dispersed yttrium oxide particles and verifying the irradiation resistance of 15-15Ti alloy in the future work.

Acknowledgments

This work was supported by the National Major R&D Project (2017YFB0702400). AV acknowledges support from the National Science Foundation (IRES 1358088).

Declaration of competing interest

The authors claim no conflicts of interest.

Appendix A. Supplementary data

Supplementary data to this article can be found online at https://doi.org/10.1016/j.matchar.2020.110228.

References

[1] L.K. Mansur, A.F. Rowcliffe, R.K. Nanstad, S.J. Zinkle, W.R. Corwin, R.E. Stoller, Materials needs for fusion, generation IV fission reactors and spallation neutron sources – similarities and differences, J. Nucl. Mater. 329–333 (2004) 166–172, https://doi.org/10.1016/j.jnucmat.2004.04.016.
[2] K.L. Murty, I. Charit, Structural materials for gen-IV nuclear reactors: challenges and opportunities, J. Nucl. Mater. 383 (2008) 189–195, https://doi.org/10.1016/j.jnucmat.2008.08.044.
[3] Y.D. Carlan, J.L. Bechade, P. Dubuisson, J.L. Seran, P. Billot, A. Bougault, CEA developments of new ferritic ODS alloys for nuclear applications, J. Nucl. Mater. 386–388 (2009) 430–432, https://doi.org/10.1016/j.jnucmat.2008.12.156.
[4] S. Kim, T. Shobu, S. Ohtsuka, T. Kaito, M. Inoue, M. Ohnuma, Kinetic approach for growth and coalescence of Nano-size oxide particles in 9Cr-ODS steel using high-energy synchrotron radiation X-rays in SPring-8, Mater. Trans. 50 (2009) 917–921, https://doi.org/10.2320/matertrans.MER2008439.
[5] H. Salmon-Legagneur, S. Vincent, J. Garnier, A.F. Gourgues-Lorenzon, E. Andrieu, Anisotropic intergranular damage development and fracture in a 14Cr ferritic ODS steel under high-temperature tension and creep, Mater. Sci. and Eng. A. 722 (2018) 231–241, https://doi.org/10.1016/j.msea.2018.02.102.
[6] G.R. Odette, M.J. Alinger, B.D. Wirth, Recent developments in irradiation-resistant steels, Annu. Rev. Mater. Res. 38 (2008) 471–503, https://doi.org/10.1146/annurev.matsci.38.060407.130315.
[7] S.J. Zinkle, J.L. Boutard, D.T. Hoelzer, A. Kimura, R. Lindau, G.R. Odette, M. Rieth, L. Tan, H. Tanigawa, Development of next generation tempered and ODS reduced activation ferritic/martensitic steels for fusion energy applications, Nucl. Fus. 57 (2017) 92005, , https://doi.org/10.1088/1741-4326/57/9/092005.
[8] G.R. Odette, Recent progress in developing and qualifying nanostructured ferritic alloys for advanced fission and fusion applications, Jom 66 (2014) 2427–2441, https://doi.org/10.1007/s11837-014-1207-5.
[9] A. Hirata, T. Fujita, Y.R. Wen, J.H. Schneibel, C.T. Liu, M.W. Chen, Atomic structure of nanoclusters in oxide-dispersion-strengthened steels, Nat. Mater. 10 (2011) 922, https://doi.org/10.1038/nmat3150.
[10] H. Oka, M. Watanabe, S. Ohnuki, N. Hashimoto, S. Yamashita, S. Ohtsuka, Effects of milling process and alloying additions on oxide particle dispersion in austenitic stainless steel, J. Nucl. Mater. 447 (2014) 248–253, https://doi.org/10.1016/j.jnucmat.2014.01.025.
[11] H. Oka, M. Watanabe, N. Hashimoto, S. Ohnuki, S. Yamashita, S. Ohtsuka, Morphology of oxide particles in ODS austenitic stainless steel, J. Nucl. Mater. 442 (2013) S164–S168, https://doi.org/10.1016/j.jnucmat.2013.04.073.
[12] T. Sourmail, Precipitation in creep resistant austenitic stainless steels, Mater. Sci. Tech. 17 (2001) 1–14, https://doi.org/10.1179/026708301101508972.
[13] F. Qian, S.B. Jin, G. Sha, Y.J. L, Enhanced dispersoid precipitation and dispersion strengthening in an Al alloy by microalloying with Cd, Acta Mater.. 157 (2008) 114–125.doi:https://doi.org/10.1016/j.actamat.2018.07.001.
[14] Z. Shi, F. Han, The microstructure and mechanical properties of micro-scale Y2O3 strengthened 9Cr steel fabricated by vacuum casting, Mater. Des. 66 (2015) 304–308, https://doi.org/10.1016/j.matdes.2014.10.075.
[15] M. Taneike, F. Abe, K. Sawada, Creep-strengthening of steel at high temperatures using nano-sized carbonitride dispersions, Nat 424 (2003) 294, https://doi.org/10.1038/nature01740.
[16] H. Abdizadeh, R. Ebrahimifard, M.A. Baghchesara, Investigation of microstructure and mechanical properties of nano MgO reinforced Al composites manufactured by stir casting and powder metallurgy methods: a comparative study, Compos. Part B: Engineering 56 (2014) 217–221, https://doi.org/10.1016/j.compositesb.2013.08.023.
[17] S.A. Sajjadi, H.R. Ezatpour, H. Beygi, Microstructure and mechanical properties of Al–Al2O3 micro and nano composites fabricated by stir casting, Mater. Sci. Eng. A 528 (2011) 8765–8771, https://doi.org/10.1016/j.msea.2011.08.052.
[18] J. Park, S. Hong, E. Park, K. Kim, M. Lee, C. Rhee, Microstructure and properties of SA 106B carbon steel after treatment of the melt with nano-sized TiC particles, Mat. Sci. Eng. A. 613 (8) (2014) 217–223, https://doi.org/10.1016/j.msea.2014.06.103.
[19] K. Verhiest, S. Mullens, I. De Graeve, N. De Wispelaere, S. Claessens, A. De Bremaecker, et al., Advances in the development of corrosion and creep resistant nano-yttria dispersed ferritic/martensitic alloys using the rapid solidification processing technique, Ceram. Int. 40 (2014) 14319–14334, https://doi.org/10.1016/j.ceramint.2014.06.023.
[20] Z.Y. Hong, X.X. Zhang, Q.Z. Yan, Y. Chen, A new method for preparing 9Cr-ODS steel using elemental yttrium and Fe2O3 oxygen carrier, J. Alloy Compd. 770 (2019) 831–839, https://doi.org/10.1016/j.jallcom.2018.08.196.
[21] F. Peng, H. Yang, Q. Zhang, J. Luo, D. Sun, W. Liu, G. Sun, R. Dou, X. Wang, X. Xing, Growth, thermal properties, and LD-pumped 1066 nm laser performance of Nd3+ doped Gd/YTaO4 mixed single crystal, Opt. Mater. Express. 5 (2015) 2536–2544, https://doi.org/10.1364/OME.5.002536.
[22] S. Mathur, M. Veith, R. Rapalaviciute, H. Shen, G.F. Goya, W.L. Martins Filho, et al., Molecule derived synthesis of nanocrystalline YFeO3 and investigations on its weak ferromagnetic behavior, Chem. Mater. 16 (2004) 1906–1913, https://doi.org/10.1021/cm0311729.
[23] C.L. Cui, L.B. Wu, R.Z. Wu, J.H. Zhang, M.L. Zhang, Influence of yttrium on microstructure and mechanical properties of as-cast Mg–5Li–3Al–2Zn alloy, J Alloy Compd 509 (2011) 9045–9049, https://doi.org/10.1016/j.jallcom.2011.04.030.
[24] D. Liu, S.Q. Zhang, A. Li, H.M. Wang, Microstructure and tensile properties of laser melting deposited TiC/TA15 titanium matrix composites, J Alloy Compd 485 (2009) 156–162, https://doi.org/10.1016/j.jallcom.2009.05.112.
[25] H. Springer, R.A. Fernandez, M.J. Duarte, A. Kostka, D. Raabe, Microstructure refinement for high modulus in-situ metal matrix composite steels via controlled solidification of the system Fe–TiB2, Acta Mater. 96 (2015) 47–56, https://doi.org/10.1016/j.actamat.2015.06.017.
[26] H. Ke, P. Wells, P.D. Edmondson, N. Almirall, L. Barnard, G.R. Odette, et al., Thermodynamic and kinetic modeling of Mn-Ni-Si precipitates in low-Cu reactor pressure vessel steels, Acta Mater. 138 (2017) 10–26, https://doi.org/10.1016/j.matchemphys.2017.07.083.
[27] Q. Ma, B. Li, E.B. Marin, S.J. Horstemeyer, Twinning-induced dynamic recrystallization in a magnesium alloy extruded at 450 °C, Scripta Mater 65 (2011) 823–826, https://doi.org/10.1016/j.scriptamat.2011.07.046.
[28] S.W. Xu, K. Oh-ishi, S. Kamado, F. Uchida, T. Homma, K. Hono, High-strength extruded Mg–Al–Ca–Mn alloy, Scripta Mater 65 (2011) 269–272, https://doi.org/10.1016/j.scriptamat.2011.04.026.
[29] M.R. Barnett, Twinning and the ductility of magnesium alloys, Part I: Tension twins, Mater. Sci. and Eng. A. 464 (2007) 1–7, https://doi.org/10.1016/j.msea.2006.12.037.
[30] F.J. Humphreys, W.S. Miller, M.R. Djazeb, Microstructural development during thermomechanical processing of particulate metal-matrix composites, Mater. Sci. Tech. 6 (1990) 1157–1166, https://doi.org/10.1179/mst.1990.6.11.1157.
[31] Z.Y. Chen, Z.C. Dong, C. Yu, R. Tong, Microstructure and properties of Mg–5.21Li–3.44Zn–0.32Y–0.01Zr alloy, Mater. Sci. and Eng. A. 559 (2013) 651–654, https://doi.org/10.1016/j.msea.2012.09.005.

[32] M. Vasudevan, S. Venkadesan, P.V. Sivaprasad, Influence of Ti/(C + 6/7N) ratio on the recrystallization behaviour of a cold worked 15Cr-15Ni-2.2Mo-Ti modified austenitic stainless steel, J. Nucl. Mater. 231 (1996) 231–241, https://doi.org/10.1016/0022-3115(96)00377-7.

[33] S.M. Razavi, D.C. Foley, I. Karaman, K.T. Hartwig, O. Duygulu, L.J. Kecskes, Effect of grain size on prismatic slip in Mg–3Al–1Zn alloy, Scripta Mater 67 (2012) 439–442, https://doi.org/10.1016/j.scriptamat.2012.05.017.

[34] J. Zhao, Z.Q. Li, W.C. Liu, J. Zhang, L. Zhang, Y. Tian, Influence of heat treatment on microstructure and mechanical properties of as-cast Mg–8Li–3Al–2Zn–xY alloy with duplex structure, Mater. Sci. and Eng. A. 669 (2016) 87–94, https://doi.org/10.1016/j.msea.2016.05.085.